Journal of Fluids and Structures 20 (2005) 785–800

JOURNAL OF
FLUIDS AND
STRUCTURES

www.elsevier.com/locate/jfs

Coupled finite-volume/finite-element modelling of the straight-tube Coriolis flowmeter

G. Bobovnik[a,*], N. Mole[b], J. Kutin[a], B. Štok[b], I. Bajsić[a]

[a]*Laboratory of Measurements in Process Engineering, Faculty of Mechanical Engineering, University of Ljubljana, Aškerčeva 6, SI-1000 Ljubljana, Slovenia*
[b]*Laboratory for Numerical Modelling and Simulation, Faculty of Mechanical Engineering, University of Ljubljana, Aškerčeva 6, SI-1000 Ljubljana, Slovenia*

Received 29 July 2004; accepted 13 April 2005
Available online 5 July 2005

Abstract

A coupled finite-volume (FV)/finite-element (FE) numerical model of the straight-tube Coriolis flowmeter is considered. It uses the staggered partitioned algorithm with additional pressure predictor and interfield iterations to minimize the time lag in the fluid–structure coupling procedure. The solutions were evaluated in terms of the fundamental natural frequency of the vibrating system and the corresponding phase difference between the motion of the symmetrically located sensing points on the measuring tube, which are actually exploited as the measuring effects of the Coriolis flowmeter for the fluid density and the mass flowrate, respectively. The FV/FE numerical model was validated by comparison with the solutions of the Euler beam and one-dimensional flow model, as well as with the solutions of the Flügge shell and potential flow model. The respective simulations were performed for different lengths of the measuring tube.

Keywords: Coriolis flowmeter; Fluid–structure interaction; Coupled simulation

---

1. Introduction

A fluid-conveying measuring tube that is maintained vibrating usually at its first natural frequency is the primary sensing element of the Coriolis flowmeter. Due to the fluid forces acting on the tube wall the mode shape gets altered, an effect that is exploited as the basic measurement principle for the mass flowrate. Besides that, the Coriolis flowmeter also uses variations of the tube natural frequency for the estimation of the fluid density.

In order to study the measuring and other effects of Coriolis flowmeters, several models, both analytical and numerical were employed, for the description of the fluid–structure interaction phenomena in the measuring tube. The dynamics of the tube was mostly described by beam models (Euler and Timoshenko models), and the fluid flow in the measuring tube was modelled as a one-dimensional flow. A distinction can be made among different solution strategies of the proposed numerical models; exact and approximate analytical solutions for simple meter configurations employing the Euler beam model [see, e.g., Sultan and Hemp (1989), Raszillier and Durst (1991), Kutin and Bajsić

---

[*]Corresponding author. Tel.: +386 1 4771 131; fax: +386 1 4771 118
E-mail address: gregor.bobovnik@lmps.uni-lj.si (G. Bobovnik).

0889-9746/$ - see front matter © 2005 Elsevier Ltd. All rights reserved.
doi:10.1016/j.jfluidstructs.2005.04.008

(2002)], and FE simulations for the meters with more complex geometries employing the Timoshenko beam model. These can be further subdivided into applications involving steady flows (Stack et al., 1993) and those involving pulsating flows (Belhadj et al., 2000) through a measuring tube. For the description of the shell-type Coriolis flowmeter that exploits higher circumferential modes for its operation, Kutin and Bajsić (1999) employed the Flügge shell equations and potential flow theory. [A review of different mathematical models applicable in the analysis of the fluid–structure interactions in beam and shell-type structures is offered by Païdoussis (1998) and Païdoussis (2003), respectively].

All of the above-mentioned models incorporate fairly simple flow models, which do not enable the study of velocity profile effects. A possibility to avoid solving a fully coupled model (with three-dimensional fluid flow) in study of such effects is given by the weight vector theory (Hemp, 1994). Otherwise, a first step into the CFD analysis of velocity profile effects was conducted by Bobovnik et al. (2004). Because their model does not account for the flow-induced deformations of the tube, they estimated inlet flow effects by using the integral values of fluid forces acting on the inner wall of the measuring tube. In this regard, it is our objective in this paper to present a more comprehensive coupled model of a Coriolis flowmeter, capable of capturing the actual measuring effects. This model will serve in future primarily for a detailed investigation of three-dimensional flow effects.

The numerical model we consider in this paper deals with the simplest design of the flowmeter, i.e. a straight and slender measuring tube with clamped ends that vibrates at its first lateral mode. Several different lengths of the measuring tube are analysed. The respective simulation of the coupled dynamics of the fluid and the solid domain is realized by linking the FV code Comet 2.1 for the analysis of weakly compressible turbulent fluid flow ($k-\varepsilon$ turbulent model) and FE code Abaqus 6.3 for the analysis of deformable shell structures. Numerical aspects of the employed coupling procedure were discussed in Mole et al. (2004). For purposes of building a corresponding numerical model, the free vibration of the measuring tube conveying fluid is considered in the numerical analysis presented, despite the fact that the operation of Coriolis flowmeter actually involves a forced vibration problem. This can be justified by the fact that the free vibration system is surely more prone to eventual modelling deficiencies, and hence a study of such a problem contributes to better identification of certain difficulties regarding the coupling procedure in the proposed numerical model.

Parameters that represent the key measurement characteristics of the Coriolis flowmeter (the natural frequency and the phase difference) are obtained through the results of simulations and will be observed under steady state (periodic) conditions. The numerical results are additionally compared to the solutions of the Euler beam and one-dimensional flow model, as well as with the Flügge shell and potential flow model.

Coupled fluid–structure systems have already been subject of many systematic numerical studies and, based upon them, numerical models for fluid–structure interaction can generally be classified into monolithic [see, e.g., Blom (1998), van Brummelen et al. (2003), Michler et al. (2004)] and partitioned [see, e.g., Piperno (1997), Farhat and Lesoinne (2000), Piperno and Farhat (2001)]. The monolithic methods treat the interaction of a fluid with a structure on their common interface synchronously, whereas in the case of partitioned models the structure and the fluid equations are solved in an alternate fashion with the interface conditions enforced asynchronously. Due to the sequential algorithm, the latter are characterized by delayed structural deformation, which is usually lagging by one time step. In order to minimize the time-lag effect in the staggered coupling procedure, the solution procedure used in our partitioned approach is based on the pressure predictor and additional interfield iterations in each time step of the simulation (Mole et al., 2004). The stability and accuracy issues, that are among other deficiencies and also benefits, which are characteristic of partitioned methods, commented on by Felippa et al. (2001), remain also our primary concern in the conceived partitioned analysis.

2. Model definition

The model of the Coriolis meter under discussion, which is schematically presented in Fig. 1, consists of a straight measuring tube that is clamped at both ends and vibrates in the x–z plane in the first bending mode. The tube deformations are small enough for linear elastic theory to be used. Geometric and material properties of the measuring tube are its length L, internal diameter D, wall thickness h, and density ρ_S, Young's modulus E and Poisson's ratio ν.

The fluid flow, which enters the measuring tube, is steady and it has density ρ_F and average velocity v_F, so that its mass flowrate is $q_m = \rho_F v_F \pi D^2/4$. The measuring characteristic of the mass flowrate is the phase difference $\Delta\phi$, which is experienced in the motion of two sensing points S_1 and S_2, that are located symmetrically at a distance s (Fig. 1).

The considered model also neglects the effect of the motion sensors and possible added masses of the excitation system. Furthermore, with the effect of the external excitation force being eliminated as well, the respective mechanical response analysis reduces actually to a free vibration analysis of the coupled system.

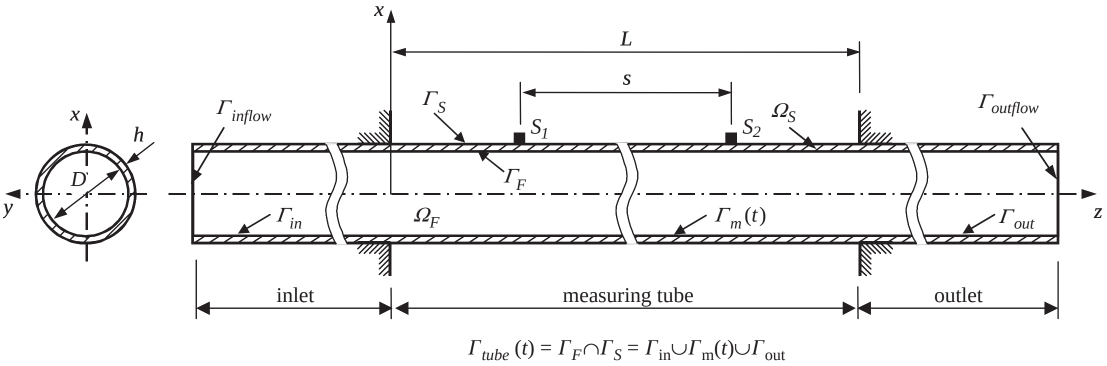

Fig. 1. Model of the Coriolis flowmeter with a straight measuring tube.

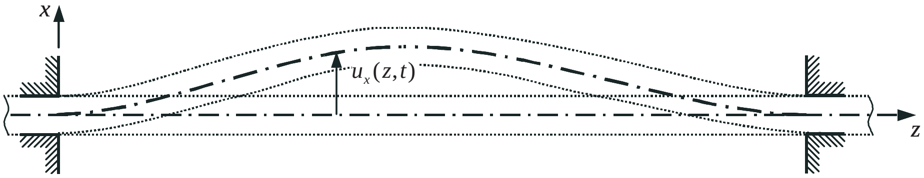

Fig. 2. Tube deflection in the Euler beam model.

3. Mathematical models used for comparison

3.1. Euler beam and one-dimensional fluid flow model

Using the Euler theory for bending of a slender beam, the measuring tube deflections will be represented by the displacement field $u_x(z,t)$, where u_x stands for the lateral deflection in the x direction (Fig. 2). The effect of the internal fluid flow is approximated by the one-dimensional plug-flow model. When considering the general model assumptions, presented in Section 2, and additionally excluding the effects of the static fluid pressure and vibration damping, the resulting equation of motion may be written as (Païdoussis, 1998)

$$EI\frac{\partial^4 u_x}{\partial z^4}+M_F v_F^2\frac{\partial^2 u_x}{\partial z^2}+2M_F v_F\frac{\partial^2 u_x}{\partial z\partial t}+(M_S+M_F)\frac{\partial^2 u_x}{\partial t^2}=0, \tag{1}$$

where EI is flexural rigidity of the tube, and M_S and M_F are the masses per unit length of the tube and the fluid, respectively. The associated boundary conditions, considering the clamped ends, are as follows:

$$u_x(z,t)=\frac{\partial u_x(z,t)}{\partial z}=0, \quad z=0\wedge z=L. \tag{2}$$

The general solution of the governing equation (1), when a harmonic response in time is assumed, may be written in complex form as follows:

$$\hat{u}_x(z,t)=\sum_{j=1}^{4}A_j e^{i\lambda_j z}e^{i\omega t}, \tag{3}$$

where ω is the angular frequency and λ_j are the eigenvalues. Both, the eigenvalues λ_j and the coefficients A_j are complex in general. By introducing the functional expression (3) for the tube deflection $\hat{u}_x(z,t)$ into Eq. (1), a characteristic polynomial in λ_j of fourth order is obtained, the solution of which are four eigenvalues λ_j $(j=1,2,3,4)$ for a distinct angular frequency ω, a frequency that yields a non-trivial solution of Eq. (1) with at least one $A_j\neq 0$. If the boundary conditions (2) are expressed in terms of (3), a homogeneous system of four linear equations in complex form is formed, with the A_j as unknowns. For non-trivial solution, setting the determinant of the coefficients equal to zero leads to a transcendental equation for the angular frequency ω, the solutions of which are the natural frequencies. The actual tube deflection is determined as the real part of the supposed complex solution (3):

$$u_x(z,t) = U_x(z)\cos(\omega t + \phi_x(z)), \tag{4}$$

where U_x is the corresponding amplitude and ϕ_x is the initial phase, that characterizes a possible time delay in the vibration response of different points. Using the phase values, the phase difference between the motion of the selected sensing points can readily be calculated.

3.2. Flügge shell and potential fluid flow model

Using the Flügge theory of a thin cylindrical shell, the measuring tube deformation will be represented by the displacements of its middle surface, i.e. the radial, circumferential and axial displacements u_r, u_θ, u_z in the respective directions of the cylindrical coordinate system (r, θ, z) (Fig. 3). Considering the general assumptions, made in Section 2, and undamped vibrations, the equations of motion may be written as (Kutin and Bajsić, 1999)

$$\begin{aligned}
&\frac{\partial^2 u_z}{\partial \xi^2} + \frac{1-v}{2}\frac{\partial^2 u_z}{\partial \theta^2} + \frac{1+v}{2}\frac{\partial^2 u_\theta}{\partial \xi \partial \theta} + v\frac{\partial u_r}{\partial \xi} + k\left(\frac{1-v}{2}\frac{\partial^2 u_z}{\partial \theta^2} + \frac{1-v}{2}\frac{\partial^3 u_r}{\partial \xi \partial \theta^2} - \frac{\partial^3 u_r}{\partial \xi^3}\right) = \gamma\frac{\partial^2 u_z}{\partial t^2},\\
&\frac{1+v}{2}\frac{\partial^2 u_z}{\partial \xi \partial \theta} + \frac{1-v}{2}\frac{\partial^2 u_\theta}{\partial \xi^2} + \frac{\partial^2 u_\theta}{\partial \theta^2} + \frac{\partial u_r}{\partial \theta} + k\left(3\frac{1-v}{2}\frac{\partial^2 u_\theta}{\partial \xi^2} - \frac{3-v}{2}\frac{\partial^3 u_r}{\partial \xi^2 \partial \theta}\right) = \gamma\frac{\partial^2 u_\theta}{\partial t^2},\\
&v\frac{\partial u_z}{\partial \xi} + \frac{\partial u_\theta}{\partial \theta} + u_r + k\left(\frac{1-v}{2}\frac{\partial^3 u_z}{\partial \xi \partial \theta^2} - \frac{\partial^3 u_z}{\partial \xi^3} - \frac{3-v}{2}\frac{\partial^3 u_\theta}{\partial \xi^2 \partial \theta} + u_r + 2\frac{\partial^2 u_r}{\partial \theta^2} + \left(\frac{\partial^2}{\partial \xi^2} + \frac{\partial^2}{\partial \theta^2}\right)^2 u_r\right)\\
&\quad = -\gamma\frac{\partial^2 u_r}{\partial t^2} + \frac{\gamma}{h\rho_t}\frac{D}{2R_m}p
\end{aligned} \tag{5}$$

where $\xi = z/R_m$, $k = h^2/(12R_m^2)$, $\gamma = \rho_S(1-v^2)R_m^2/E$, R_m is the middle-surface radius and p is the fluid pressure on the internal surface of the tube. For clamped ends, the boundary conditions are:

$$u_r(z,\theta,t) = \frac{\partial u_r(z,\theta,t)}{\partial z} = u_\theta(z,\theta,t) = u_z(z,\theta,t) = 0; \quad z = 0 \wedge z = L. \tag{6}$$

The effect of the internal fluid flow is approximated by linearized potential flow theory. The solution of thus defined problem follows the travelling wave procedure presented in Païdoussis (2003). If a general solution for the tube displacements, which are harmonic in time and periodic circumferentially, is written in complex form as

$$\begin{aligned}
&\hat{u}_r(z,\theta,t) = \sum_{j=1}^{8}\hat{u}_{r,j}(z,\theta,t) = \sum_{j=1}^{8} A_j \mathrm{e}^{\mathrm{i}\lambda_j z}\cos n\theta\, \mathrm{e}^{\mathrm{i}\omega t}, \quad \hat{u}_\theta(z,\theta,t) = \sum_{j=1}^{8} B_j \mathrm{e}^{i\lambda_j z}\sin n\theta\, \mathrm{e}^{\mathrm{i}\omega t}\\
&\hat{u}_z(z,\theta,t) = \sum_{j=1}^{8} C_j \mathrm{e}^{\mathrm{i}\lambda_j z}\cos n\theta\, \mathrm{e}^{\mathrm{i}\omega t},
\end{aligned} \tag{7}$$

the fluid pressure on the tube surface, excluding the effect of static pressure, can be written as

$$p = -\rho_F \sum_{j=1}^{8} \frac{\mathrm{I}_n(\lambda_j D/2)}{\mathrm{dI}_n(\lambda_j r)/\mathrm{d}r|_{r=D/2}}\left(\frac{\partial^2 \hat{u}_{r,j}}{\partial t^2} + 2v_F\frac{\partial^2 \hat{u}_{r,j}}{\partial t\, \partial z} + v_F^2\frac{\partial^2 \hat{u}_{r,j}}{\partial z^2}\right). \tag{8}$$

Here, $I_n(\,)$ is the nth order modified Bessel function of the first kind and n is the circumferential wave number, which is $n = 1$ for the bending mode under discussion. Although the derivation of the fluid pressure does not include the realistic

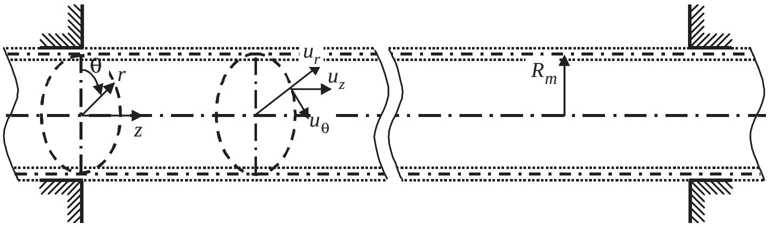

Fig. 3. Tube displacements in the Flügge shell model.

boundary conditions at the tube ends, that are $u_r = 0$ for $z<0$ and $z>L$, this simplification may have an influence only for relatively short tubes, as commented upon by Shayo and Ellen (1974).

Introducing the assumed solutions for displacements and pressure (Eqs. (7) and (8)) into governing equations (5) yields a homogeneous system of three linear equations with A_j, B_j, and C_j as complex unknowns. For non-trivial solutions, the determinant of the coefficients has to vanish, thus yielding a transcendental equation in λ_j. For eight boundary conditions (6), eight values of λ_j (and eight solutions B_j/A_j, C_j/A_j) are of interest. It is appropriate to choose the eigenvalues with the smallest modulus, because they contribute the most to the formation of the mode shapes (Païdoussis, 2003). Finally, if the boundary conditions (6) are expressed in terms of the functional expressions (7), a homogeneous system of eight linear equations in A_j is formed. By setting the determinant of the coefficients equal to zero for non-trivial solutions, one obtains a transcendental equation in the angular frequency ω, with natural frequencies as respective solutions. The phase difference between the motion of the selected sensing points will be determined from the phase variations of the radial displacement u_r at $\theta = 0$, which can be written in the familiar form

$$u_r(z,t)\big|_{\theta=0} = U_r(z)\,\cos(\omega t + \phi_r(z)). \tag{9}$$

This simplification is reasonable because $u_\theta|_{\theta=0} = 0$ and amplitudes of u_z are relatively small.

4. Coupled fluid–structure interaction model

4.1. Fluid dynamics problem

4.1.1. Governing domain equations

The fluid flow through the tube is assumed as isothermal, Newtonian and weakly compressible. Its three-dimensional spatial distribution ($\mathbf{x} \in \Omega_F$) and time evolution ($t>0$) are governed by the conservation of mass and momentum principles, which will be represented in their integral form. For a fluid with the density ρ_F and absolute velocity $\mathbf{v}_F$ of the particles in the fluid domain Ω_F, the continuity and momentum equations read as follows:

$$\frac{\partial}{\partial t}\int_{\Omega_F} \rho_F \mathrm{d}\Omega + \int_{\Gamma_F} \rho_F(\mathbf{v}_F - \mathbf{v}_S)\cdot\mathbf{n}\,\mathrm{d}\Gamma = 0, \tag{10}$$

$$\frac{\partial}{\partial t}\int_{\Omega_F} \rho_F \mathbf{v}_F\,\mathrm{d}\Omega + \int_{\Gamma_F} \rho_F \mathbf{v}_F(\mathbf{v}_F - \mathbf{v}_S)\cdot\mathbf{n}\,\mathrm{d}\Gamma = \int_{\Gamma_F} \mathbf{T}_F\cdot\mathbf{n}\,\mathrm{d}\Gamma + \int_{\Omega_F} \mathbf{f}_F\,\mathrm{d}\Omega. \tag{11}$$

In the above equations the constraints on the fluid flow, as imposed by the motion of the surrounding tube wall, and prescribed by the respective surface velocities $\mathbf{v}_S$ on the fluid domain boundary Γ_F (**n** being the normal vector at the boundary Γ_F) are taken fully into account. Vector $\mathbf{f}_F$ in the momentum equation (11) stands for the volume forces that act inside the domain Ω_F, and $\mathbf{T}_F$ is the resulting stress tensor, which is composed of the viscous stress tensor $\mathbf{T}_f$ and Reynolds stress tensor $\mathbf{T}_t$:

$$\mathbf{T}_F = \mathbf{T}_f + \mathbf{T}_t \tag{12}$$

The viscous stress tensor $\mathbf{T}_f$ is defined as

$$\mathbf{T}_f = \mu(\mathrm{grad}\mathbf{v}_F + (\mathrm{grad}\mathbf{v}_F)^{\mathrm{T}}) - \frac{2}{3}\mu\,\mathrm{div}\,\mathbf{v}_F\,\mathbf{I} - p\mathbf{I} \tag{13}$$

with p being the fluid pressure, **I** the unit tensor and μ the dynamic viscosity, while the Reynolds stress tensor $\mathbf{T}_t$, which results from fluid turbulence, is given according to the assumed k-ε turbulence model by

$$\mathbf{T}_t = \mu_t(\mathrm{grad}\,\mathbf{v}_F + (\mathrm{grad}\,\mathbf{v}_F)^{\mathrm{T}}) - \tfrac{2}{3}(\mu_t\,\mathrm{div}\,\mathbf{v}_F + \rho_F\,k)\mathbf{I}. \tag{14}$$

In the above, the turbulent viscosity μ_t depends on the turbulent kinetic energy k and its dissipation rate ε, the quantities that are obtained from a solution of two additional transport equations (Pope, 2000).

4.1.2. Initial and boundary conditions

For the moment, let us assume that both the domain Ω_F and its boundary Γ_F are known in time. As we are mainly interested in the determination of the fluid response during a vibration of the tube under some prescribed inlet flow conditions, the initial velocity field $\mathbf{v}_F^0$ and the stress field $\mathbf{T}_F^0$ in the fluid may be assumed identical to the steady state fields that correspond to the fully developed velocity profiles, reached in the tube at rest. Those can be actually obtained upon a preliminary simulation of the flow in a sufficiently long tube under considered inflow conditions and prescribed ambient pressure at the outflow boundary. In a simulation of the vibrating tube, the same fully developed velocity profile $\mathbf{v}_F^0$ can be set as the prescribed boundary condition at the inflow boundary, while at the outflow boundary the ambient pressure p^0 is imposed. No-slip conditions were presumed at the fluid–tube interface.

Considering the geometry of the investigated measuring tube and physical nature of the associated boundary conditions, the boundary Γ_F can be decomposed into three parts: Γ_{inflow}, $\Gamma_{\text{tube}}(t)$ and Γ_{outflow} (Fig. 1) with respective boundary conditions for the assumed viscous flow written as:

$$\begin{aligned}
&\mathbf{v}_F(\mathbf{x},t) = \mathbf{v}_F^0(\mathbf{x}), \quad \mathbf{x} \in \Gamma_{\text{inflow}},\\
&p(\mathbf{x},t) = p^0(\mathbf{x}), \quad \mathbf{x} \in \Gamma_{\text{outflow}},\\
&\mathbf{v}_F(\mathbf{x},t) = \mathbf{v}_S^*(\mathbf{x},t), \quad \mathbf{x} \in \Gamma_{\text{tube}}(t),\\
&\mathbf{v}_S(\mathbf{x},t) = 0, \quad \mathbf{x} \in \Gamma_{\text{inflow}} \cup \Gamma_{\text{outflow}}.
\end{aligned} \tag{15}$$

Here, we also assumed that the velocity $\mathbf{v}_S^*$ of the external cylindrical boundary of the considered fluid volume domain is prescribed.

4.2. Structural dynamics problem

4.2.1. Governing domain equations

The measuring tube of the considered Coriolis flowmeter is analysed as a deformable shell structure occupying a solid domain Ω_S, with Γ_S being the corresponding boundary. The three-dimensional spatial distribution ($\mathbf{x} \in \Omega_S$) and time evolution ($t > 0$) of the respective mechanical response is governed by conservation of momentum principles as well, but for convenience, a variational integral formulation will be used. The corresponding equation of motion can be derived by Hamilton's variational principle, which may be written as

$$\int_{t_1}^{t_2} \delta\left(W_p - W_k\right)\,\mathrm{d}t = 0 \tag{16}$$

where W_p and W_k are, respectively, the total potential energy and the total kinetic energy of the considered moving structure.

The total potential energy W_p is expressed as a sum of the strain energy corresponding to the actual deformation of the shell, and the potential of the load corresponding to the actually applied conservative external forces. Considering the nature of the case investigated, only surface forces $\mathbf{q}_S$, acting upon the moving shell boundary through the respective displacement field $\mathbf{u}_S$, are taken into account in the load potential, thus yielding the following integral expression for the total potential energy:

$$W_p = \frac{1}{2}\int_{\Omega_S} \mathbf{T}_S : \boldsymbol{\varepsilon}_S\,\mathrm{d}\Omega - \int_{\Gamma_S} \mathbf{q}_S \cdot \mathbf{u}_S\,\mathrm{d}\Gamma. \tag{17}$$

In the above equation $\boldsymbol{\varepsilon}_S$ and $\mathbf{T}_S$ are, respectively, the strain and the stress tensor in the deformed shell structure.

The total kinetic energy W_k of the moving structure can be written as

$$W_k = \frac{1}{2}\int_{\Omega_S} \rho_S(\mathbf{v}_S \cdot \mathbf{v}_S)\,\mathrm{d}\Omega, \tag{18}$$

where ρ_S is the density of the tube material and $\mathbf{v}_S$ is the velocity field of the structure.

4.2.2. Initial and boundary conditions

For the moment let us assume that external actions, either in a form of the applied surface forces $\mathbf{q}_S^*$ or imposed displacements $\mathbf{u}_S^*$ on the boundary Γ_S, are known in time. Being interested in the determination of the structural response during a vibration of the tube under some prescribed inlet flow conditions, the initial configuration Ω_S^0 is assumed identical to the tube configuration at rest. For a complete kinematic definition of the straight vibrating tube at time $t = 0$, however, respective velocities $\mathbf{v}_S^0$ and accelerations $\mathbf{a}_S^0$ must be given. The corresponding initial mechanical state is assumed unstressed and unstrained; therefore $\mathbf{T}_S^0 = \boldsymbol{\varepsilon}_S^0 = \mathbf{0}$. In view of the above assumed external actions the respective boundary conditions are written as

$$\begin{aligned}\mathbf{u}_S(\mathbf{x},t) &= \mathbf{u}_S^*(\mathbf{x},t), \quad \mathbf{x} \in \Gamma_S^u(t),\\ \mathbf{T}_S(\mathbf{x},t)\cdot\mathbf{n}(\mathbf{x},t) &= \mathbf{q}_S^*(\mathbf{x},t), \quad \mathbf{x} \in \Gamma_S^T(t),\end{aligned} \tag{19}$$

where both, $\mathbf{u}_S^*$ and $\mathbf{q}_S^*$, are known prescribed quantities.

4.3. Coupled fluid–structure dynamics problem

At the common interface ($\Gamma_F \cap \Gamma_S$) in a coupled fluid–structure problem, which will be denoted by Γ_{tube} (Fig. 1), none of the problem variables is given explicitly. Since at that interface the stress–displacement compatibility between the field variables of the respective systems in contact must be respected, this relation is established implicitly by imposing kinematic and contact stress constraints. With **n** denoting the normal vector at the interface $\Gamma_{\text{tube}}(t)$ these constraints are formulated, always assuming viscous flow, as follows:

$$\begin{aligned}\mathbf{T}_F(\mathbf{x},t)\cdot\mathbf{n}(\mathbf{x},t) &= \mathbf{T}_S(\mathbf{x},t)\cdot\mathbf{n}(\mathbf{x},t),\\ \mathbf{u}_F(\mathbf{x},t) &= \mathbf{u}_S(\mathbf{x},t), \quad \mathbf{x} \in \Gamma_{tube}(t).\end{aligned} \tag{20}$$

4.4. Numerical model of the coupled fluid–structure problem

In view of an approximate solution to the above-stated coupled fluid–structure problem, we use two different numerical approaches. For a solution of the fluid dynamics problem the FVM is used, while the structural dynamics problem is considered within the FEM framework. The computer simulation of the fluid–structure interaction in the measuring tube of the considered Coriolis flowmeter will be thus performed by an appropriate coupling technique exploiting the computed results of each individual problem. The commercially available codes Comet 2.1 (FVM) and Abaqus 6.3 (FEM) will be used, respectively, for solution of the specified tasks.

Briefly, the Comet code uses the FVM to transform the governing differential equations into finite-difference equations. The unsteady terms are discretized in accordance with a first-order two-time-level implicit scheme, while the convective and diffusive terms are approximated by using the second-order central difference scheme. The convergence in a single time step is reached when the sum of the absolute residuals for all equations falls by five orders of the magnitude.

In the Abaqus code, which solves a dynamic problem in accordance with the FEM, the solution is sought by dividing the total response time of the system into time intervals, called time steps. The dynamic equilibrium equations are solved and the values of the unknowns are determined at the end of a time step, based on the knowledge of their values at the beginning of the considered time step. The Newmark formulae are used for implicit time displacement and velocity integration.

In the numerical model of the vibrating Coriolis flowmeter the fluid and the structural domain are discretized in accordance with the applied numerical approaches (Fig. 4). The discretization is performed in such way that the two meshes, based respectively on the FE and the FV discretization, coincide at the fluid–structure interface. Consequently, the finite-volume mesh follows in time the motion of the tube, which is actually modelled as a shell. In order to keep the same finite-volume mesh topology as time progresses, the displacements of internal nodes are correspondingly adjusted in each time step.

4.4.1. Coupled fluid–structure simulation strategy

In principle, considering the decomposition of the fluid-conveying measuring tube into two interacting domains—the structure and the fluid domain (Fig. 4), and different solvers used for the computation of the respective structural and fluid response, the coupled computation can be performed iteratively, considering fluid–structure interaction and mutual fulfilment of energy balance at the common interface. The iteration loop starts with the computation of the structural response, performed on the undeformed tube upon prescribed initial kinematic conditions and loads, as obtained by the steady state flow conditions in the tube at rest. The induced vibration yields, in the first time step of the coupled simulation, the displacement and velocity vectors of the tube. With the new tube geometry and computed velocity vectors imposed as the boundary conditions in the fluid flow simulation, the respective pressure and velocity response of the fluid for the same time interval are obtained as the response of the fluid to the induced vibration of the tube. In the next time step, considering the computed kinematic state of the structure from the previous time step as actual initial conditions, and with application of the fluid forces (obtained by the respective pressure distribution that is

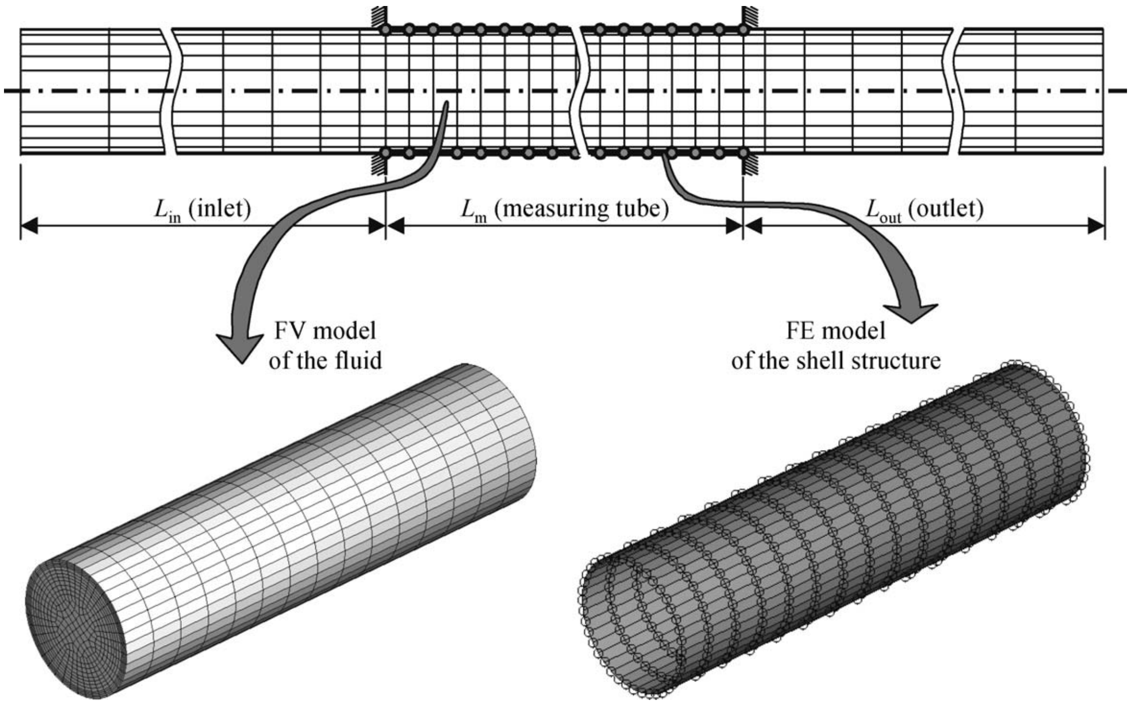

Fig. 4. FV/FE numerical model of fluid-conveying tube.

computed in the fluid at the end of the previous time step) as actual boundary conditions, the displacement and velocity vectors of the tube are determined anew. The described cyclic procedure of alternate exchange of the data between the two computational codes follows the following pattern: with given initial and boundary conditions, data are created within one code to be used in the other code as initial and boundary conditions, the computation thus yielding the respective data to be used in the subsequent numerical step as updated initial and boundary conditions for the other code.

The procedure just described works in principle, but in its elementary version it needs rather a long time to converge. Further numerical investigations have proven that a rather fast convergence of the numerical response can be obtained by relying for the approximation of the fluid stress tensor for a considered time step upon the results of the previous three time steps, and by applying the fluid load in a smooth way (Mole et al., 2004). In particular, with the gradual application of the fluid load to the solid structure being accomplished within the first 120 time steps, a converged vibration is thus obtained in approximately eight cycles. To minimize the time lag that is introduced by the staggered coupling procedure, additional interfield iterations were employed in each time step of the simulation.

4.5. Estimation of the natural frequency and the phase difference

Considering that the basic measuring effects of the investigated Coriolis flowmeter are the established natural frequency of the measuring tube and the phase difference exhibited in the motion of two symmetrically positioned sensing points S_1 and S_2 (see Fig. 1), those are in fact the quantities we have focused on, and represent actually the final results of our numerical simulation. Both quantities were estimated from the velocity responses at the sensing points position ($v_{S_1,x}, v_{S_2,x}$) using the digital signal processing in LabVIEW environment.

Since we were dealing with free oscillation of the tube, the velocity responses (signals) at the sensing points were expected to be sinusoidal with exponentially decaying amplitude. For subsequent signal normalization, the resulting signals were first approximated, using the Levenberg–Marquardt fitting algorithm, by the following function:

$$v_A(t) = V_A \sin(2\pi f_A(1-\delta_A^2)t + \phi_A)\mathrm{e}^{-2\pi f_A \delta_A t} + V_{DC}, \tag{21}$$

where V_A is the amplitude, f_A is the frequency, ϕ_A is the phase, δ_A is the damping factor and V_{DC} is the DC value of the signal. In the following step, the values obtained with this approximation were used for normalization of the DC value of the signal and its decaying amplitude, using the following expression:

$$\tilde{v}_{S,x}(t) = \frac{v_{S,x}(t) - V_{DC}}{V_A \mathrm{e}^{-2\pi f_A \delta_A t}}. \tag{22}$$

Next, the low-pass filter (cut-off frequency $\approx f_A + 40\,\mathrm{Hz}$) was applied to both responses with the intention of eliminating the higher frequency components and the high-frequency noise, respectively. After conducting these operations on the total signal length, the signals were split into segments of two periods, in steps of half a period from the beginning towards the end of the signal. Splitting the signals into segments allowed us further to observe the transient response of the considered quantities and to assess whether the results converge to a steady state solution.

The initial and the terminal intersection with the time axis, considering linear interpolation, were determined for each investigated segment of the velocity response, and the corresponding frequency f characterizing the observed segment was calculated directly from the obtained time values at the intersections.

The phase for each segment was obtained employing the DFT algorithm, and the phase difference $\Delta\phi$ was calculated as the difference between the phase values of the corresponding segments.

5. Numerical simulation results and comparative analysis

This section discusses the results that have been performed in the context of the coupled fluid–structure modelling, as presented in Section 4. Explicitly, the natural frequency of damped vibration (corresponding to the first lateral mode shape of the measuring tube) and the phase difference between the two sensing points positioned symmetrically to the tube centre, have been considered. The results of numerical simulations were further compared with the solutions of the two analytical models, presented in Section 3. For a fully developed inlet velocity profile with an average fluid velocity of 5 m/s, the simulations were carried out for five particular cases, differing in the length of the measuring tube ($L/D = 10,15,20,25$ and 30), while D was kept constant at 0.02 m and the lengths of the inlet and outlet section of the fluid domain remained fixed at 0.4 m. All other properties of the measuring tube and the fluid, which are listed in Table 1, remained unaltered for all the simulations conducted.

As in the numerical simulation the measuring part of the tube is forced into oscillation by prescribing an initial velocity field corresponding to the first vibration mode, the respective kinematic conditions considered in the analysis are as follows:

$$\begin{aligned} &\mathbf{u}_S(\mathbf{x},0) = 0, \\ &\mathbf{v}_S(\mathbf{x},0) = \beta_0 \mathbf{A}(\mathbf{x}), \quad \mathbf{x} \in \Omega_S, \\ &\mathbf{a}_S(\mathbf{x},0) = 0, \end{aligned} \tag{23}$$

with the amplitude vector field $\mathbf{A}(\mathbf{x})$ being determined independently in accordance with the tube first natural mode shape of the clamped–lamped measuring tube. The scalar β_0 isconstant multiplier, its magnitude being adjusted to meet the maximum deflection requirement, which is set for the tube with the fluid at a value of about $D/10$.

In addition to the effects of the numerical grid density and the time step size, the evolution of the observed parameters (the natural frequency and the phase difference) is investigated further in this section. In the end, comparisons of the natural frequency and the phase difference for the three models considered (Euler beam and one-dimensional flow; Flügge shell and potential flow; and coupled numerical model) are presented.

Table 1
Tube geometry and physical properties

Geometry			Tube (Ti)		
L_m	(m)	0.2…0.6	ρ_S	(kg/m^3)	4510
L_{in}	(m)	0.4	E	(GPa)	102.7
L_{ou}	(m)	0.4	ν	—	0.34
D	(m)	0.02	Fluid (H_2O)		
h	(m)	5×10^{-4}	ρ_F	(kg/m^3)	1000
s	(m)	$L_m/2$	μ	(Pa s)	1.002×10^{-3}

5.1. Discretization of the computational domain

First, the influence of the space and time discretization on convergence of the solution and its accuracy was investigated. This investigation was performed for a particular case, actually for the parameter values given in Table 1 and for the tube with the ratio $L/D = 20$. To find out the influence of applying different numerical grid densities, three different lengths of elements in the axial direction of the measuring tube were presumed: 10, 5 and 2.5 mm. For the discretization of the cross-section of the fluid domain an unaltered grid pattern was applied. In all cases the length and the number (40) of circumferential boundary elements are equal for the fluid and for the solid domain, thus perfect matching of the boundary elements across the interface is ensured, and no additional interpolation procedure is needed at the data exchange between the two domains. For the time integration a time step equal to 1.72×10^{-5} s was applied, which corresponds to approximately 140 time steps per period of vibration. The values of the natural frequency and the phase difference after 2300 time steps (approximately 16 periods of vibration) were compared for the assumed spatial discretizations (see Fig. 5). As expected, the largest deviation of the results is evidenced for the coarsest grid (10 mm), but the frequency (and the phase difference) obtained on the grids with the element lengths of 5 and 2.5 mm, deviates by for 0.06% and 0.13%, respectively.

Next, the effect of two different time step sizes was investigated for the computational grid with element length of 5 mm.Time step sizes were set to approximately 1/140 and 1/70 of the oscillation period that yields, respectively, $\delta t_1 = 1.72 \times 10^{-5}$ s and $\delta t_2 = 3.44 \times 10^{-5}$ s. In both cases the absolute values of the natural frequency and the phase difference deviated by less than 0.1%, but the vibration damping factor in the case with the larger time step was twice as large as in the first case, an issue that is further discussed in Section 5.2.

Based on the results obtained, a the computational grid with elements of 5 mm length in the axial direction of the tube and the time step size of approx. Oscillation period of 1/40 was selected for further simulations. The time step sizes selected with respect to the actual ratio L/D of the measuring tube are given in Table 2.

5.2. Evolution of the natural frequency and the phase difference

In Fig. 6 is displayed the velocity response at the sensing point S_1, positioned on the inlet half of the measuring tube as indicated in Fig. 1, for the measuring tube of $L/D = 20$. Observing this velocity response we must be aware that its initial part does not represent the true physical transient response of the mechanical system, but corresponds to the smooth application of the fluid pressure and the adopted initial conditions, which were selected so as to assure a steady state response in as short a computational time as possible. It is obvious that the initial velocity, as well as the natural

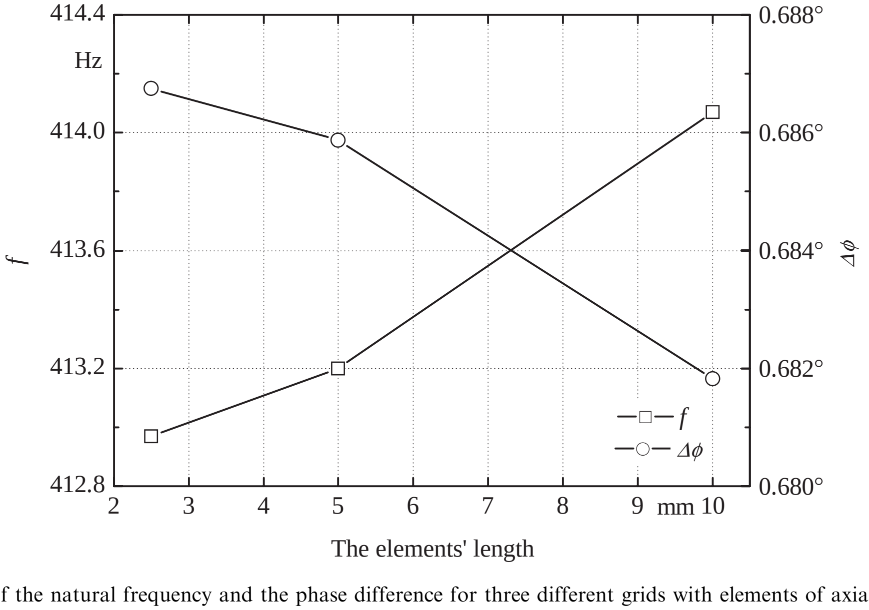

Fig. 5. Variation of the natural frequency and the phase difference for three different grids with elements of axial length 2.5, 5 and 10 mm, respectively ($L/D = 20$).

Table 2
Time step values with respect to the ratio L/D of the measuring tube

L/D	10	15	20	25	30
δt (s)	4.76×10^{-6}	1.00×10^{-5}	1.72×10^{-5}	2.65×10^{-5}	3.75×10^{-5}

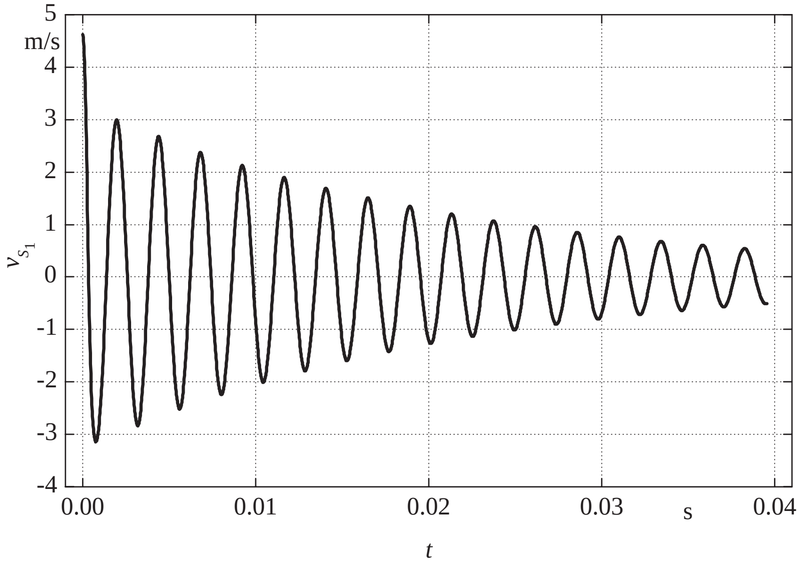

Fig. 6. The variation of the velocity signal at sensing point S_1 obtained with numerical model ($L/D = 20$).

frequency, are reduced to the value characteristic of the fully coupled system already during the first period of vibration. This is quite in accordance with the computationally exerted fluid pressure on the solid interface. The fluid pressure is actually applied to its full amount gradually, over a time interval corresponding to some portion of the vibration period.

The damping factor (δ) of the vibration of the tube conveying fluid, determined from the velocity response at the sensing points, considering the same case presented in Fig. 6, is equal to 1.8×10^{-2}, whereas the damping of the empty tube equals to 4.5×10^{-3}. As already emphasized in the previous subsection, the magnitude of damping of the fluid–solid system depends strongly on the time steps size used in a transient simulation. As commented for example by Piperno and Farhat (2001) and Piperno (1997), damping or amplification of a simulated response, obtained with partitioned staggered algorithms, can be attributed to improper energy conservation on the interface between the two domains. In the case under consideration it was found that the damping factor increased practically proportionally with the time step size, whereas applying the second-order three-time-level integration scheme for the fluid solver reduced the damping factor by approximately 30%, but immensely prolonged the computational time. With respect to the case of the empty tube it is then mostly the numerical procedure, and to a certain degree also the effect of the presence of the fluid in the tube, that contribute to the augmentation of the system damping.

In Figs. 7 and 8 the evolutions of the natural frequency and the phase difference (calculated using the algorithm presented in Section 4.5) are displayed along the signal length of 2300 time steps for the measuring tube with $L/D = 20$. The natural frequency is higher during the first periods and reaches the steady state value after approximately 8 vibration cycles in the observed case. The higher values of the frequency experienced in the early stages are due to the coupling algorithm procedure; namely, as explained by Mole et al. (2004), the total pressure resulting from the flow simulation is entered in the solid solver in the full amount only after 120 time steps, which means that in the early stages of the simulation the tube responds as being empty or filled with a fluid of lower density; consequently, in the initial phase, higher natural frequencies than later in the simulation process are shown. A similar instability in the phase difference in the initial stages of the simulation, which originates from the same cause, is visible in Fig. 8, and disappears after 8 periods of vibration.

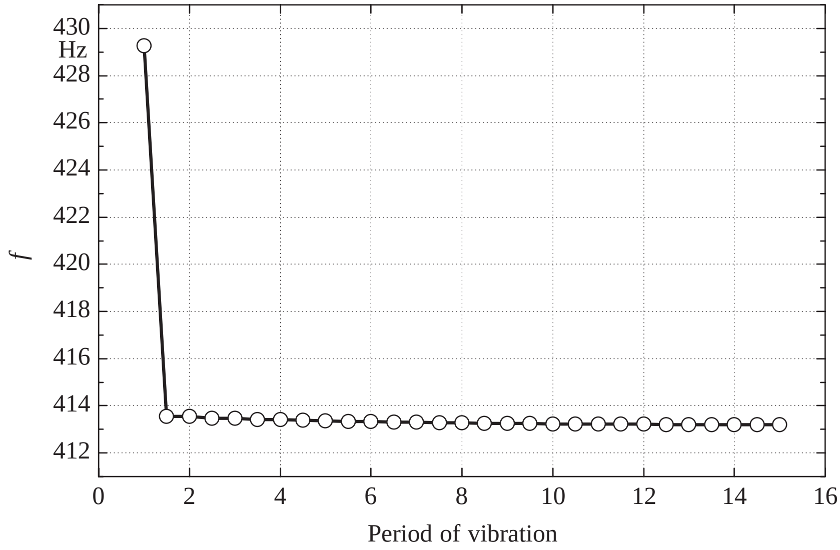

Fig. 7. Evolution of the calculated natural frequency ($L/D = 20$).

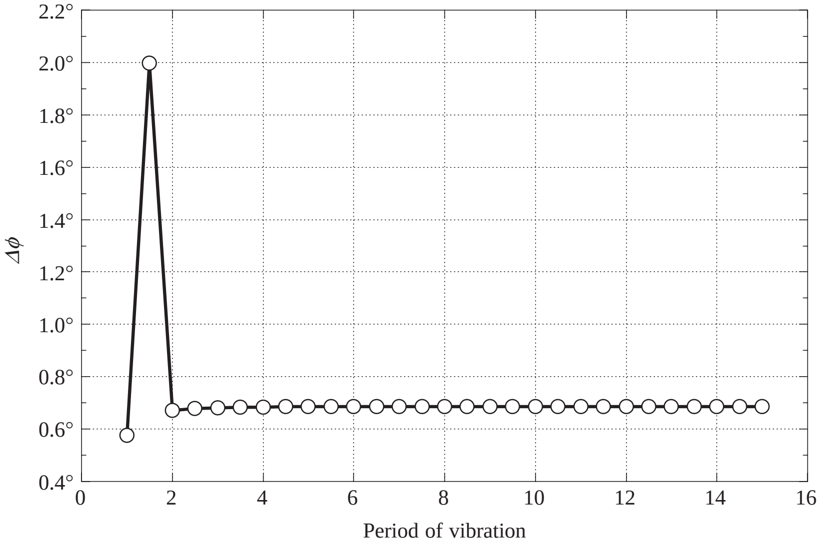

Fig. 8. Evolution of the calculated phase difference ($L/D = 20$).

5.3. Steady state values of the natural frequency and the phase difference

In this part of the paper, the results obtained from the coupled fluid–structure numerical model are compared with the analytical solutions obtained, respectively, with the Euler beam and one-dimensional flow model and the Flügge shell and potential flow model. To achieve the steady state regime, the numerical simulations were conducted for 2300 time steps (approximately 16 periods of vibration). The natural frequency and the phase difference between the sensing points S_1 and S_2 were determined as the average of the last four calculated values, and their numerical stability is estimated by the maximum deviation from the average value. The frequencies and the phase differences are stabilized within 0.02% and 0.10%, respectively, except in the case of $L/D = 10$, where the frequency is stable within 0.10% and the phase difference within 1.40%.

Before proceeding to the discussion of the results, we have to emphasize that the solutions of comparative models refer to undamped vibrations (contrary to our numerical results that are obtained from the damped responses). This, however, does not importantly influence the presented results. The natural frequency of damped vibration is lower than the natural frequency of undamped vibration by the factor $(1-\delta^2)^{1/2}$ (approximately 0.02% in our simulations). The expected influence on the phase difference was analysed by Kutin and Bajsić (2002) and is proved to be of the same order of magnitude as for the natural frequency.

In Fig. 9 the natural frequencies for different lengths of the measuring tube are presented for the three models compared. In the given scale the natural frequency obtained with the numerical simulations seems to coincide with the Flügge shell and potential flow model; therefore, the deviation of the results relative to the Euler beam and one-dimensional flow model for both the Flügge shell and potential flow and the coupled numerical model, is presented in Fig. 10 separately. The deviation of the natural frequency relative to the Euler beam and one-dimensional

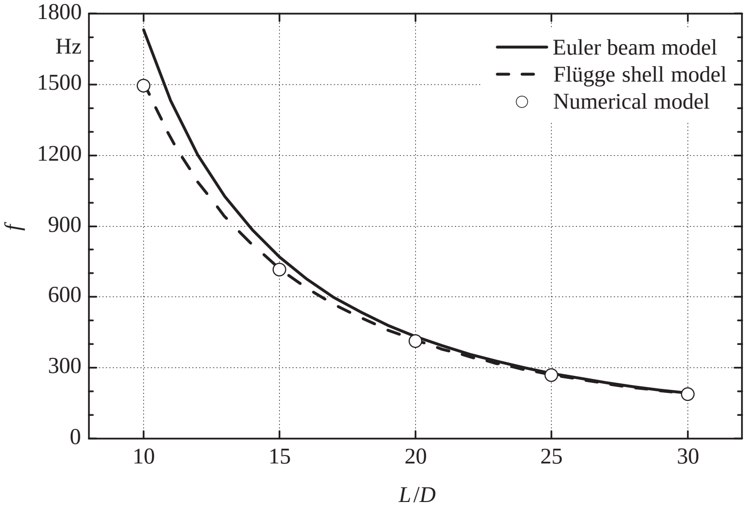

Fig. 9. Comparison of the natural frequency obtained with the employed models (Euler beam and one-dimensional flow, Flügge shell and potential flow, and coupled numerical model) for various lengths of the measuring tube.

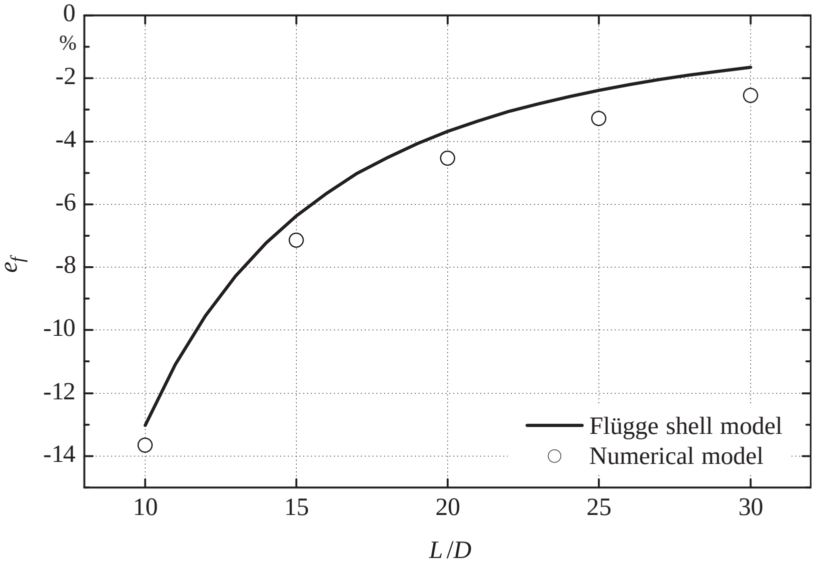

Fig. 10. Deviations of the natural frequency for the Flügge shell and potential flow model and the coupled numerical model relative to the Euler beam and one-dimensional flow model for various lengths of the measuring tube.

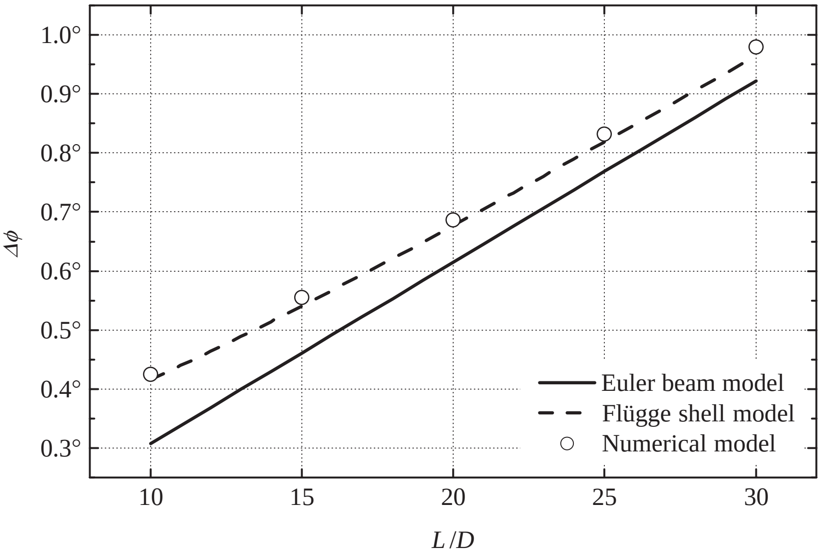

Fig. 11. Comparison of the phase difference obtained with the employed models (Euler beam and one-dimensional flow, Flügge shell and potential flow, and coupled numerical model) for various lengths of the measuring tube.

flow model is defined as

$$e_f = \left(\frac{f - f_E}{f_E}\right), \tag{24}$$

where f_E represents the value of the natural frequency of the observed system according to the Euler beam and one-dimensional flow model.

It is obvious that the natural frequency obtained with the proposed numerical model follows the same trend as the values obtained from the Flügge shell and potential flow model (the difference between them is a bit less than 1% over the whole observed range), but on the other hand it is also evident, that the Euler beam and one-dimensional flow model predicts much higher first natural frequencies for the tubes with a smaller ratio of L/D (almost up to 14%). In contrast, for the highest ratio of L/D, this difference is smaller than 3% for all three models.

Next, the values of the phase difference for the observed models are presented in Fig. 11. The values from all three models follow the same trend, with the Euler beam and one-dimensional flow model predicting the lowest and the proposed numerical model the highest values of the phase difference. To investigate these differences a little more in detail, we introduce the deviation relative to the Euler model and one-dimensional flow (analogous to equation (24) for the frequency):

$$e_{\Delta\phi} = \left(\frac{\Delta\phi - \Delta\phi_E}{\Delta\phi_E}\right), \tag{25}$$

where $\Delta\phi_E$ is the value of the phase difference obtained with the Euler beam and one-dimensional flow model.

As seen in Fig. 12 the values predicted with the Flügge shell and potential flow model and with the numerical model are in a very good agreement with each other (approximately within 2.5% for the shortest two tubes, and approximately 1.5% for other simulated geometries), but differ noticeably from the results of the Euler beam and one-dimensional flow model. For the shortest measuring tube considered ($L/D = 10$) the Euler beam and one-dimensional flow model predicts more than 35% lower values of the phase difference. Indeed, such dimensions of the measuring tubes are not common in the industrial design of Coriolis flowmeters, but even for tubes with a greater L/D the Euler beam and one-dimensional flow model still underpredicts the phase difference for more than 5%.

6. Conclusions

A partitioned numerical approach for treating the fluid–structure interaction in the measuring tube of a Coriolis flowmeter is presented. Computationally coupled analysis of the three-dimensional discretized model was realized by

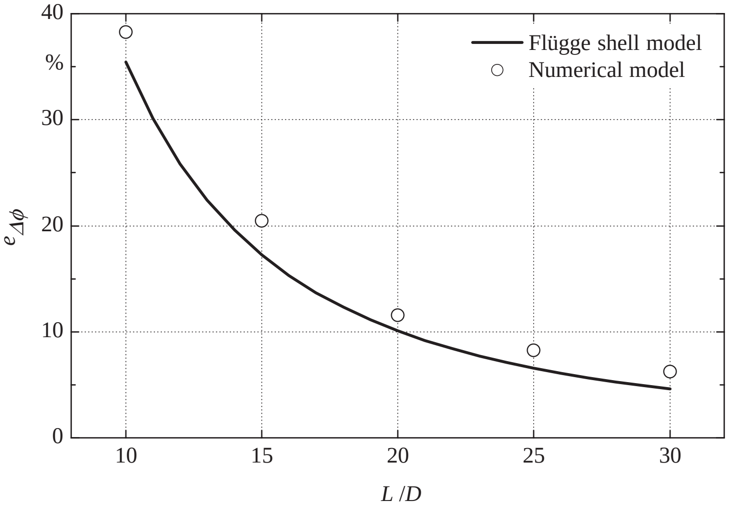

Fig. 12. Deviations of the phase difference for the Flügge shell and potential flow model and the coupled numerical model relative to the Euler beam and one-dimensional flow model for various lengths of the measuring tube.

coupling of a FV code for the fluid flow and a FE code for the structure. The analysis of the computed results (the natural frequency and the phase difference between the sensing points positioned symmetrically on the inlet and outlet halves of the tube, respectively) is based on comparison with the analytical solutions of (i) the Euler beam and one-dimensional flow model and (ii) the Flügge shell and potential flow model. At a constant mass flow rate of the viscous fluid, the natural frequencies and the phase differences were observed for five different lengths of a tube with the same cross-sectional area, i.e. the same diameter and the same wall thickness.

In order to determine the natural frequency, the free vibration of the measuring tube was simulated. Due to the energy loss on the coupling interface, excessive damping is predicted, which is mainly due to the employment of the two-time-level implicit time integration scheme and the time step size used. However, it was found that the increased damping of the system, using the presented algorithm (Section 4.5), does not have a significant influence on the estimation of the natural frequency and the phase difference, which are the key results of the presented study.

The comparison of the natural frequencies for the considered three models showed similar trends in all cases. The results of the Euler beam and one-dimensional flow model predicted the highest frequencies (up to 14% higher than the other two models for $L/D = 10$). The natural frequencies obtained with the Flügge shell and potential flow model and the numerical model deviate over the entire observed range of tube lengths ($L/D = 10$, 15, 20, 25 and 30) by less than 1%. Similar observations apply for the phase difference, where the Euler beam and one-dimensional flow model predicts the lowest values of the phase differences for all the tubes, while the corresponding numerical model yields the highest ones. The deviation between them is approximately 35% for the shortest tube ($L/D = 10$) and about 6% for the longest tube ($L/D = 30$). The results of the Flügge shell and potential flow model coincide much better with predictions of the numerical simulations (deviation is approximately 2% over the entire range of the tube lengths observed).

The authors have also tested the Timoshenko beam and one-dimensional flow model (Stack et al., 1993). As expected that model performs better than the Euler beam and one-dimensional flow model and its results (for the considered slender tube configuration) deviate from those of the proposed numerical model of the same order of magnitude as those of the Flügge shell and potential flow model. On the basis of the results presented herein and the study of Bobovnik et al. (2004), where it was established that the actual fluid forces are in very good agreement with the one-dimensional fluid flow assumption for the slender-type tube configuration, we can claim that significant differences between the models do not lie in the different treatment of the fluid flow, but originate from different approaches used in modelling of the structural domain.

The numerical model presented incorporates a three-dimensional analysis of fluid flow in a deformable shell structure and, with regard to its modelling assumptions, is certainly believed to be the best among the compared models. In future, it can be employed for the study of three-dimensional flow effects (velocity profile effects) or other fluid parameters (temperature, pressure, compressibility, etc.) and can be realized for any arbitrary design specifications of industrial flowmeters.

References

Belhadj, A., Cheesewright, R., Clark, C., 2000. The simulation of Coriolis meter response to pulsating flow using a general purpose F.E. code. Journal of Fluids and Structures 14, 613–634.

Blom, F.J., 1998. A monolithical fluid–structure interaction algorithm applied to the piston problem. Computer Methods in Applied Mechanics and Engineering 167, 369–391.

Bobovnik, G., Kutin, J., Bajsić, I., 2004. The effect of flow conditions on the sensitivity of the Coriolis flowmeter. Flow Measurement and Instrumentation 15, 69–76.

Farhat, C., Lesoinne, M., 2000. Two efficient staggered algorithms for the serial and parallel solution of the three-dimensional nonlinear aeroelastic problems. Computer Methods in Applied Mechanics and Engineering 182, 499–515.

Felippa, C.A., Park, K.C., Farhat, C., 2001. Partitioned analysis of coupled mechanical systems. Computer Methods in Applied Mechanics and Engineering 190, 3247–3270.

Hemp, J., 1994. The weight vector theory of Coriolis mass flowmeters. Flow Measurement and Instrumentation 5, 247–253.

Kutin, J., Bajsić, I., 1999. Characteristics of the shell-type Coriolis flowmeter. Journal of Sound and Vibration 228, 227–242.

Kutin, J., Bajsić, I., 2002. An analytical estimation of the Coriolis meter's characteristics based on modal superposition. Flow Measurement and Instrumentation 12, 345–351.

Michler, C., Hulshoff, S.J., van Brummelen, E.H., de Borst, R., 2004. A monolithic approach to fluid–structure interaction. Computers and Fluids 33, 839–848.

Mole, N., Bobovnik, G., Kutin, J., Štok, B., Bajsić, I., 2004. Coupled Fluid–structure Simulation of Coriolis Flowmeter. In: Proceedings of the Fourth International Conference on Engineering Computational Technology, Lisbon, Portugal.

Païdoussis, M.P., 1998. Fluid–structure Interactions: Slender Structures and Axial Flow, Vol. 1. Academic Press, London.

Païdoussis, M.P., 2003. Fluid–structure Interactions: Slender Structures and Axial Flow, Vol. 2. Elsevier Academic Press, London.

Piperno, S., 1997. Explicit/implicit fluid/structure staggered procedures with a structural predictor and fluid subcycling for 2D inviscid aeroelastic simulations. International Journal for Numerical Methods in Fluids 25, 1207–1226.

Piperno, S., Farhat, C., 2001. Partitioned procedures for the transient solution of coupled aeroelastic problems—Part II: energy transfer analysis and three-dimensional applications. Computer Methods in Applied Mechanics and Engineering 190, 3147–3170.

Pope, S.B., 2000. Turbulent Flows. Cambridge University Press, Cambridge.

Raszillier, H., Durst, F., 1991. Coriolis-effect in mass flow metering. Archive of Applied Mechanics 61, 192–214.

Shayo, L.K., Ellen, C.H., 1974. The stability of finite length circular cross-section pipes conveying inviscid fluid. Journal of Sound and Vibration 37, 535–545.

Stack, C.P., Garnett, R.B., Pawlas, G.E., 1993. A finite element for the vibration analysis of fluid-conveying Timoshenko beam. In: the 34th AIAA/ASME Structures, Structural Dynamics and Materials Conference (AIAA-93-1552-CP), La Jolla, CA, USA.

Sultan, G., Hemp, J., 1989. Modelling of Coriolis mass flowmeter. Journal of Sound and Vibration 132, 473–489.

Van Brummelen, E.H., Hulshoff, S.J., De Borst, R., 2003. Energy conservation under incompatibility for fluid–structure interaction problems. Computer Methods in Applied Mechanics and Engineering 192, 2727–2748.